

AN EMERGING FLUX TRIGGER MECHANISM FOR CORONAL MASS EJECTIONS

P. F. CHEN^{1,2} AND K. SHIBATA¹

Received 2000 May 12; accepted 2000 July 24

ABSTRACT

Observations indicate that reconnection-favored emerging flux has a strong correlation with coronal mass ejections (CMEs). Motivated by this observed correlation and based on the flux rope model, an emerging flux trigger mechanism is proposed for the onset of CMEs, using two-dimensional magneto-hydrodynamic (MHD) numerical simulations: when such emerging flux emerges within the filament channel, it cancels the magnetic field below the flux rope, leading to the rise of the flux rope (owing to loss of equilibrium) and the formation of a current sheet below it. Similar global restructuring and a resulting rise motion of the flux rope occur also when reconnection-favored emerging flux appears on the outer edge of the filament channel. In either case, fast magnetic reconnection in the current sheet below the flux rope induces fast ejection of the flux rope (i.e., CME). It is also shown that the nonreconnecting emerging flux, either within the filament channel or on the outer edge of the channel, makes the flux rope move down, i.e., no CMEs can be triggered. Although the present two-dimensional model can not provide many details of the largely unknown three-dimensional processes associated with prominence eruptions, it shows some observational features such as the height-time profile of erupting prominences. Most importantly, our model can well explain the observed correlation between CMEs and the reconnection-favored emerging flux.

Subject headings: Sun: corona — Sun: flares — magnetic fields — MHD

1. INTRODUCTION

Coronal mass ejections (CMEs) are by far the most striking manifestation of solar activity seen in the solar corona. They attracted a lot of interest by their own extreme characteristics (mass, energy, etc.), as well as their relation with other solar activities (prominence eruptions, solar flares, etc.) and geomagnetic activities. The most interesting aspect is that of their origin (Hundhausen 1999). Now it is clear that CMEs are not the simple by-products of solar flares (such as shock waves), and we believe that both CMEs and flares are produced by the same global MHD process. It has often been argued that many CMEs are not related to flares (Kahler 1992; Gosling 1993). However, recent *Yohkoh* observations have revealed that many non-flare-related CMEs are associated with soft X-ray arcades (Hiei, Hundhausen, & Sime 1993; Hudson, Haisch, & Strong 1995), which appear to be similar to flare arcades (Tsuneta et al. 1992; Hanaoka et al. 1994), and they might both be produced by fast reconnection. In this sense, CMEs are closely related to “flares” (Shibata 1996), and both CMEs and “flares” (normal flares and soft X-ray arcades, i.e., reconnection) may be coupled with each other (Ugai 1982). There are some arguments that MHD provides an inaccurate description of reconnection (e.g., Hesse et al. 1999). This is true for magnetospheric reconnection, since the size of the magnetosphere is not so different from the microscopic plasma scale (such as ion gyroradius or ion inertial length). However, as far as the solar corona dynamics is concerned, the MHD approach is justified since its microscopic plasma scale is much smaller than the size of coronal phenomena like flares and CMEs.

As pointed out by Feynman & Hundhausen (1994), many solar activities, including CMEs, are involved in evolving

magnetic structure (EMS). Various types of EMS have been investigated to study the destabilization of the coronal structure (see also Tandberg-Hanssen 1995). Magnetic arcades with shear motion are widely studied. It is found that after large enough shear, the closed magnetic arcades would asymptotically approach the open field, while resistive instability can result in the eruption (Mikić, Barnes, & Schnack 1988; Biskamp & Welter 1989; Finn, Guzdar, & Chen 1992; Mikić & Linker 1994). However, for the pure shear motion, it may take an unrealistically long time for the shear to exceed the critical value. Besides, the magnetic shear in some observational reports is, in fact, due to the emergence of a twisted flux rope (Kurokawa 1987, 1996). Converging motion of the magnetic arcades, by which a filament may be formed (Martin 1990), can also lead to the destabilization of the filament structure (van Ballegooijen & Martens 1989; Inhester, Birn, & Hesse 1992; Forbes & Priest 1995). This can be easily understood as the increase of the magnetic pressure near the solar surface. The results by Wu & Guo (1997) showed that the emergence of a strong enough magnetic bubble below a helmet can destabilize the helmet to form a CME. Guo, Wu, & Tandberg-Hanssen (1996) simulated a similar process but with opposite magnetic field direction in the bubble. In both cases, helmet eruption is induced. This is not surprising since in the latter case the oppositely-directed magnetic field lines in the bubble reconnect with the magnetic field in the helmet so as to produce a new magnetic rope similar to the emerging magnetic bubble in Wu & Guo (1997).

The emerging flux model is a fascinating mechanism for both solar flares (Heyvaerts, Priest, & Rust 1977; Shibata, Nozawa, Matsumoto 1992; Yokoyama & Shibata 1996) and CMEs. Sheared magnetic fields at the photosphere, which are believed to be related to CMEs, might be explained as the result of either photospheric motion or the emerging twisted flux. Statistical studies by Feynman & Martin (1995) show that many CMEs are correlated to

¹ Kwasan Observatory, Kyoto University, Kyoto 607-8471, Japan; shibata@kwasan.kyoto-u.ac.jp.

² Department of Astronomy, Nanjing University, Nanjing 210093, China; CHENPF@NJU.EDU.CN.

emerging flux. Their research also indicates that the emerging flux favorable for magnetic reconnection with preexisting field has a very high probability of triggering filament eruptions (and CMEs), which is confirmed by Wang & Sheeley (1999). Based on numerical simulations, this paper proposes an emerging flux trigger mechanism for CMEs, which provides a physical explanation for the above observational results.

The theoretical model and numerical method are introduced in § 2, the numerical results are described in § 3, discussions and conclusion are given in § 4.

2. MODEL AND NUMERICAL METHOD

2.1. Initial Model

In the consideration of Aly's constraint (Aly 1991; Sturrock 1991), Low & Smith (1993) and Low (1994) proposed that a magnetic configuration with a detached magnetic bubble (flux rope) is an ideal candidate for the pre-CME structure, i.e., the so-called three-part structure. The cavity with a bright core was found recently by *Yohkoh* observation (Hudson et al. 1999). Moreover, the twisted flux rope model was also confirmed in many CMEs observations by *SOHO/LASCO* (Chen et al. 1997; Dere et al. 1999; Wood et al. 1999). Besides the possibility of storing more energy, the flux rope model explains the filament channel and the widely existing "inverse-polarity" filaments (Low 1999). For this reason, we use "flux rope" rather than "filament" when it is concerned.

To get the magnetic configuration with a detached flux rope, our pre-CME model consists of three separate current elements in a two-dimensional Cartesian plane, as shown in Figure 1: line current centered at the point $(0, h)$ with finite radius r_0 , its image current below the photosphere, and a background potential field, similar to that in Forbes (1990). However, the background field is quadrupolar in our case, which is produced by four line currents below the photosphere, i.e., at four positions $(\pm 1.5, -0.3)$ and $(\pm 0.3, -0.3)$, with the directions being "−", "+", "+", and "−" in sequence. For flux rope ejection, the quadrupolar field is more favorable than a bipolar magnetic field (Forbes, Isenberg, & Priest 1994). The quadrupolar structure of the

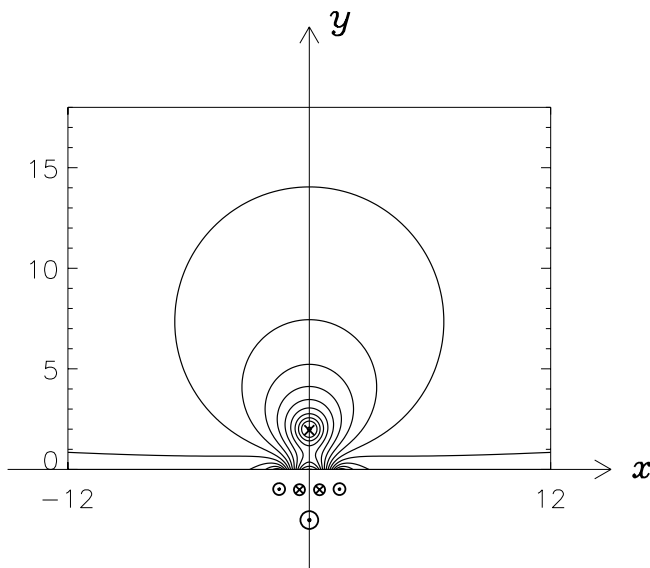


FIG. 1.—Initial magnetic configuration and its source currents

CME source is an important discovery by *SOHO* observations (Howard et al. 1997). It also can often be seen in the magnetogram from Kitt Peak observations (see Fig. 2).

The initial magnetic configuration is expressed as $\psi = \psi_b + \psi_i + \psi_t$, where the background field (ψ_b) and the magnetic components of the image current (ψ_i) and of the line current (ψ_t) have the following forms:

$$\psi_b = c \ln \frac{[(x + 0.3)^2 + (y + 0.3)^2][(x - 0.3)^2 + (y + 0.3)^2]}{[(x + 1.5)^2 + (y + 0.3)^2][(x - 1.5)^2 + (y + 0.3)^2]}, \quad (1)$$

$$\psi_i = -\frac{r_0}{2} \ln [x^2 + (y + h)^2], \quad (2)$$

$$\psi_t = \begin{cases} r^2/(2r_0), & r \leq r_0; \\ r_0/2 - r_0 \ln(r_0) + r_0 \ln(r), & r > r_0. \end{cases} \quad (3)$$

The magnetic flux function ψ is related to the magnetic field (\mathbf{B}) by $\mathbf{B} = \nabla \times (\psi \hat{e}_z)$; the coefficient c in the formula of ψ_b represents the strength of the background field; $r = [x^2 + (y - h)^2]^{1/2}$; $h = 2$; $r_0 = 0.5$. In this configuration, the magnetic field (\mathbf{B}) decreases as $\sim y^{-3}$ along the height y .

Uniform temperature $T = T_0$ is assumed. Initial density is distributed as

$$\rho/\rho_0 = \begin{cases} 1 + \frac{2}{\beta} \left(1 - \frac{r^2}{r_0^2}\right), & r \leq r_0; \\ 1, & r > r_0, \end{cases} \quad (4)$$

where β is the ratio of gas to magnetic pressures. Similar to that in Forbes (1990), the initial gas pressure ($P = \rho R_0 T$) balances the magnetic force within the current filament only when the image current and the background field are absent. Gravity and gas pressure both are important for CMEs (Low 1996); however, since we emphasize the onset process, which is magnetic in nature in our model, the gravity is neglected here. It is noted that an actual three-dimensional flux rope would most likely be curved and would therefore be subject to extra Lorentz forces which are not considered in the present two-dimensional model.

According to the observational results by Feynman & Martin (1995), two types of reconnection-favored emerging flux can trigger CMEs, i.e., within the filament channel and on the outer edge of the channel, as shown in Figure 2. Two

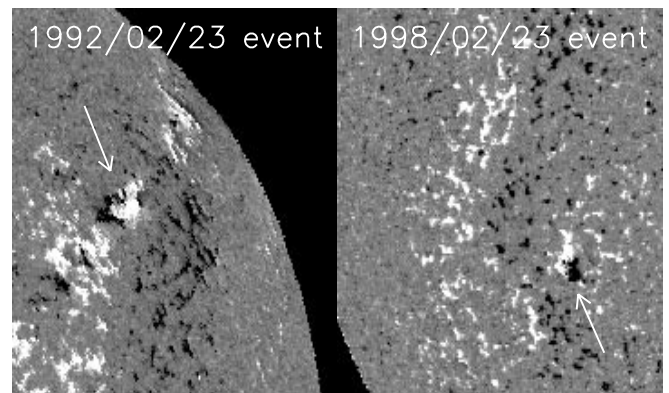


FIG. 2.—Two categories of reconnection-favored emerging flux: within the filament channel (left panel) and on the outer edge of the filament channel (right panel)

cases (A and B) are investigated here: in case A, the flux emergence appears near the magnetic neutral line $x = 0$, and in case B, it appears on the outer edge of the filament channel.

2.2. Numerical Method

Two-dimensional time dependent compressible resistive MHD equations are shown below, which are numerically solved by a multistep implicit scheme (Hu 1989):

$$\frac{\partial \rho}{\partial t} + \nabla \cdot (\rho \mathbf{v}) = 0, \quad (5)$$

$$\frac{\partial \mathbf{v}}{\partial t} + (\mathbf{v} \cdot \nabla) \mathbf{v} + \frac{1}{\rho} \nabla P - \frac{1}{\rho} \mathbf{j} \times \mathbf{B} = 0, \quad (6)$$

$$\frac{\partial \psi}{\partial t} + \mathbf{v} \cdot \nabla \psi - \eta \Delta \psi = 0, \quad (7)$$

$$\frac{\partial T}{\partial t} + \mathbf{v} \cdot \nabla T + (\gamma - 1) T \nabla \cdot \mathbf{v} - \frac{2(\gamma - 1)\eta}{\rho \beta_0} \mathbf{j} \cdot \mathbf{j} = 0, \quad (8)$$

where $\gamma = 5/3$ is the ratio of specific heats; the five independent variables are density (ρ), velocity (v_x, v_y), magnetic flux function (ψ), and temperature (T); $\mathbf{j} = \nabla \times \mathbf{B}$ is the current density. The characteristic values for ρ , T are $\rho_0 = 1.67 \times 10^{-12} \text{ kg m}^{-3}$, $T_0 = 10^6 \text{ K}$, respectively. β is chosen to be 0.01, so that the corresponding Alfvén speed v_A is 1818 km s^{-1} . Since heat conduction and gravity are neglected here, the dimensionless results are independent of the length scale, L_0 , as indicated in Chen et al. (1999a). Here we might as well consider $L_0 = 10^5 \text{ km}$, therefore the Alfvén transit time τ_A equals 55 s. The resistivity η , which is distributed outside the initial current filament, has the following current-density dependent form:

$$\eta = \begin{cases} \eta_0 \min \left(1, \left| \frac{j_z}{j_c} \right| - 1 \right), & |j_z| \geq j_c; \\ 0 & |j_z| < j_c, \end{cases} \quad (9)$$

where $\eta_0 = 0.02$, j_z is the current density, $j_c = 0.5$ is the critical value of j_z , beyond which the resistivity is assumed

to be excited. It is well known that the current dependent resistivity model as equation (9) can lead to fast reconnection (Tajima & Shibata 1997).

The dimensionless size of the simulation box is $-12 \geq x \geq 12$ and $0 \geq y \geq 18$. The domain is discretized by 161×181 grid points, which are uniformly distributed in the y -direction and nonuniformly along the x -direction. The bottom of the simulation area is a line-tying boundary, where all quantities except T are fixed outside the flux emerging region, T is determined by equivalent extrapolation. The other three boundaries are assumed to be open ones.

As done by Forbes & Priest (1984), the flux emergence is realized by changing the boundary magnetic field. Here we change the value of ψ until $t = t_e = 200\tau_A$, i.e., $\psi(x, 0, t) = \psi(x, 0, 0) + \psi_e t/t_e$ ($t \leq t_e$), in the local region $|x - x_0| \leq 0.3$, where x_0 represents the location of the emerging flux. After $t = t_e$, the bottom boundary is fixed except T as before.

Note that in equation (1), the coefficient c is determined by trial and error in order to guarantee that the flux rope center approximately keeps stable for long enough time. In our simulations, c is set to be 2.5628.

3. NUMERICAL RESULTS

3.1. Onset of the CME

In case A, the emerging flux, $\psi_e = 11 \cos(\pi x/0.6)$, appears near the neutral line, i.e., $|x| \leq 0.3$, with direction opposite to the ambient coronal field. Magnetic reconnection occurs as the new flux emerges, which leads to partial magnetic cancellation, and therefore the decrease of magnetic pressure. The magnetized plasma at both sides (left and right to the null point) is seen to move inward, as indicated in Figure 3. As the frozen-in field lines accumulate near the y -axis, the current density (j_z) near the neutral line increases nearly exponentially with time until $t = 62\tau_A$, and especially, after $t = 52\tau_A$, the maximum current density is larger than that in the initial current filament. Meanwhile, the flux rope moves upward.

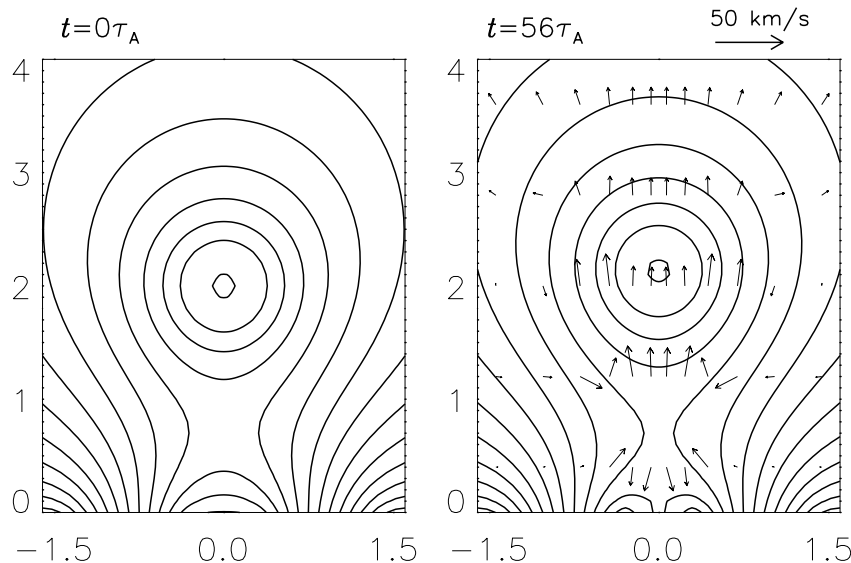


FIG. 3.—Onset of the flux rope in response to the reconnection-favored emerging flux within the filament channel (case A). Solid lines represent the field lines, arrows correspond to the velocity.

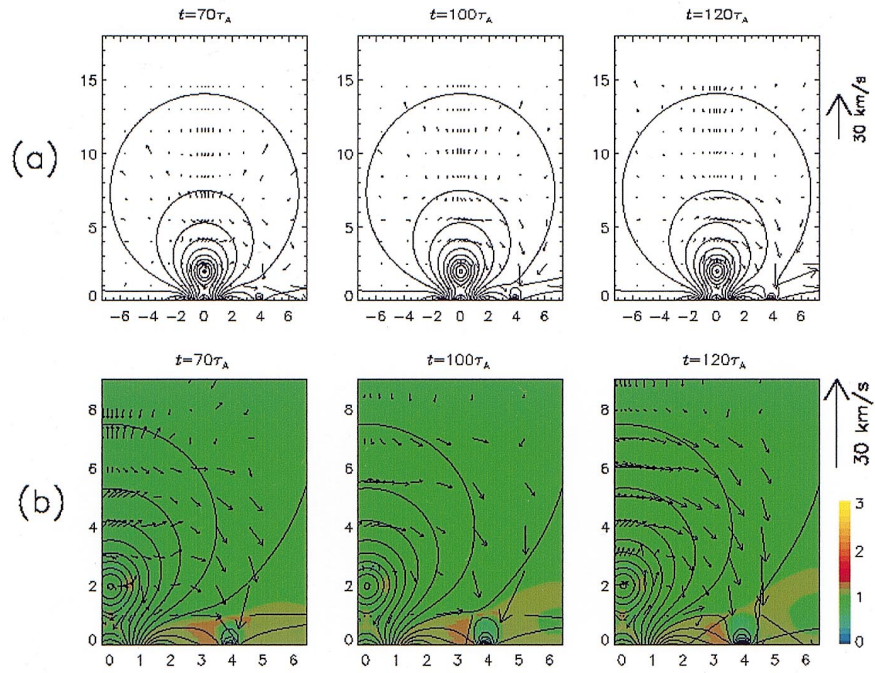


FIG. 4.—Onset of the flux rope in response to the reconnection-favored emerging flux on the outer edge of the filament channel (case B). The upper panel shows the global evolution of magnetic (*lines*) and velocity (*arrows*) fields; the lower panel amplifies the local region near the emerging flux, where the temperature distribution (*color map*) indicates the “precursor” before the onset of the flux rope.

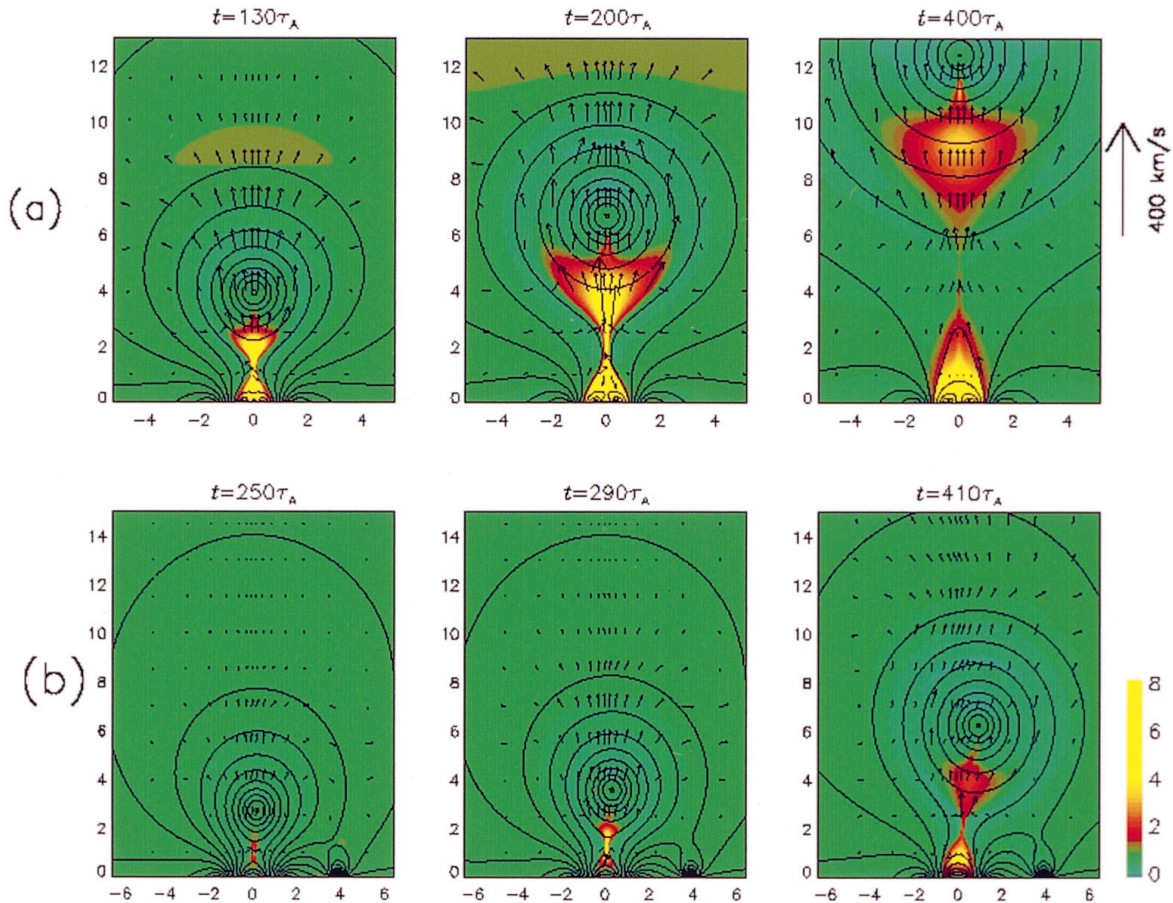


FIG. 5.—Resistive evolution in case A (*upper panel*) and case B (*lower panel*). The solid lines correspond to the magnetic field, the arrows to the velocity, and the color map to the temperature.

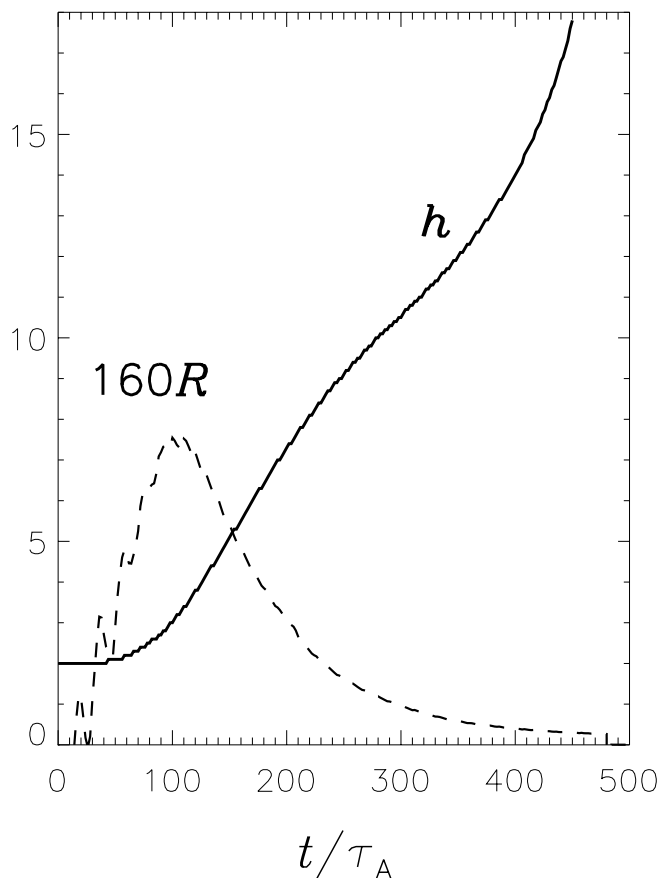


FIG. 6.—Time profiles of the reconnection rate (R) and the height of the flux rope center (h) in case A. The solid line is for h , and the dashed line is for R .

In case B, the emerging flux is introduced within $|x - 3.9| \leq 0.3$ at the bottom, with $\psi_e = -25 \cos(\pi(x - 3.9)/0.6)$. As clearly shown in Figure 4, reconnection between the emerging flux and the coronal field heats the local plasma to high temperature. The reconnected field lines, which are firstly connected to the left-hand side of the emerging region, are diverted to its right-hand side and are ejected outward along with reconnection outflow. The flux rope follows the reconnection inflow, and moves upward. After the onset of the flux rope ejection, the local region below the flux rope becomes evacuated, therefore, magnetized plasma at both sides (left and right to the null point) is driven by the gradient gas pressure to move inward. Similar to case A, a current sheet is formed below the flux rope.

3.2. Resistive Evolution

It was seen in § 3.1 that, in both cases (A and B), there occur the onset of the flux rope ejection and the formation of a current sheet below the flux rope. The current in the sheet has the same direction as that in the flux rope, and then sheds a downward Lorentz force on the flux rope, which stops it from continual ejection. If resistivity sets in, the current sheet will be dissipated, and therefore the flux rope can escape from the solar surface, especially being accelerated by the reconnection outflow (upward jet).

As the current density in the current sheet exceeds the critical value j_c , resistivity is self-consistently introduced, then magnetic reconnection is triggered. Figure 5 depicts

the evolution of the magnetic field, velocity, and temperature in both cases (upper panel for case A, lower panel for case B). In both cases, reconnection occurs at an X-point. The plasma above the X-point is accelerated by the magnetic tension force of the reconnected field lines. The upward jet (outflow) collides with the flux rope to form an upward-propagating reverse fast shock, by which the flux rope is pushed away until it moves out of the top boundary. Below the X-point, the reconnection outflow collides with the line-tied magnetic loops, and a cusp-shaped structure with high temperature is clearly seen, which is the typical soft X-ray feature of LDE (long-duration event) flares, as numerically simulated in detail by Chen et al. (1999b). In case A, it is clearly seen that plasma heating appears above the erupting flux rope, which is contributed to by the piston-driven shock. Figure 6 shows the time profiles of the reconnection rate (R) and the height of the flux rope center in case A, where it can be seen that the flux rope is accelerated rapidly near $t = 50\tau_A$. After $t = 100\tau_A$, it rises approximately with constant velocity. This kind of height profile is often obtained in the observations of flare-related CMEs (Howard et al. 1997), as well as numerically reproduced by Magara, Shibata, & Yokoyama (1997). Moreover, the reconnection rate (R) reaches its maximum at $t \sim 100\tau_A$, which is much delayed from the start of the flux rope ejection but is close to the maximum acceleration phase of the flux rope. The reconnection rate corresponds to the electric field and is directly related to the hard X-ray process. Figure 6 implies that the hard X-ray maximum is delayed from the onset of the CME and close to its acceleration phase, which is consistent with observations of H α filament eruptions (e.g., Kahler et al. 1988) and X-ray plasmoid ejection (e.g., Ohya & Shibata 1997; Tsuneta 1997).

4. DISCUSSION AND CONCLUSION

4.1. Emerging Flux Trigger Mechanism

As suggested by observations (Feynman & Martin 1995), two types of emerging flux with reconnection-favored direction can trigger filament eruptions (and then CMEs). One is within the filament channel, the other is on the outer edge of the channel. Our two cases (A and B) correspond to these two categories, respectively. In case A, the emerging flux reconnects with the magnetic loops below the flux rope and leads to partial magnetic cancellation, which decreases the local magnetic pressure. Then, the magnetized plasma at the two sides is pressed by the resulting magnetic pressure gradient to move inward, and the frozen-in field lines accumulate near the y -axis to form a current sheet. Owing to the low- β of the corona, the cross-field current is concentrated in a thin layer near the neutral line. At the same time, the inflow pushes the flux rope upward, leading to the onset of the flux rope ejection. In case B, the emerging flux reconnects with the overlying magnetic field of the flux rope. After reconnection, the two laterally interacting magnetic loops evolve to a small inner loop and a large outer loop. The locally concave outer loop is ejected outward along with the reconnection outflow. This expansion can also be understood as follows: since the magnetic pressure decreases as $\sim y^{-3}$ along the height, the magnetic pressure gradient makes the flux rope have a tendency to escape from the solar surface, which is stopped by the downward magnetic tension force. After the reconnection between the emerging flux and the overlying coronal field, the magnetic

structure is rearranged, and the reconnected outer loop becomes less bent, i.e., the magnetic tension force decreases and then, the flux rope is accelerated upward. Thereafter, the surrounding plasma below the flux rope moves inward, as inferred from the conservation of mass. Field lines move along with the inflow and accumulate near the y -axis; then a current sheet is formed below the flux rope. Note that the maximum current density is limited by the numerical mesh, especially in the strongly asymmetric case B.

Such a newly formed current sheet attracts the flux rope and stops it from continual motion until the flux rope reaches new equilibrium. If fast reconnection is inhibited below the flux rope, the rise velocity of flux rope becomes too slow (even stops) to explain actual observations, as already revealed by many researchers (e.g., Forbes 1990; Choe & Lee 1996), i.e., it seems that no “global nonequilibrium” exists in two-dimensional cases, where magnetic reconnection is necessary for eruptions (Amari et al. 1997). When resistivity is introduced into the current sheet, the current is dissipated, and our numerical simulations show a rapid ejection of the flux rope, as is also shown by Mikić & Linker (1994). Below the current sheet, a cusp structure is formed with high temperature, which is considered to be the signature of solar flares or arcades in soft X-ray (SXR).

It has been observed that weak SXR activity often precedes the flash phase of solar flares (Datlowe, Elcan, & Hudson 1974) or the linearly extrapolated starting time of the CMEs (Harrison et al. 1985). The localized heating due to the reconnection between the emerging flux and the overlying magnetic field in our numerical results may account for the weak SXR activity, i.e., the precursor, as clearly seen in the lower panel of Figure 4. Our numerical simulations further indicate that the reconnection-favored emerging flux either cancels the magnetic fields below the flux rope or rearranges the global structure of the overlying coronal field, which leads to the loss of equilibrium of the flux rope and the formation of a current sheet below the flux rope. The following magnetic reconnection in the newly formed current sheet leads to the eruption of the CME and the solar flare. In this sense, the emerging flux acts only as a trigger for the CMEs. Compared to previously considered models discussed in § 1, it is found that for eruptions the important point is the formation of a current sheet, which can be produced by the shear motion (e.g., Mikić, Barnes, & Schnack 1988), converging motion (e.g., Forbes & Priest 1995), or localized magnetic reconnection (e.g., our model).

As a comparison, we simulate the opposite situations, i.e., flux emergence with reconnection-unfavored direction both within the filament channel (the opposite of case A) and on the outer edge of the channel (the opposite of case B). As shown in Figure 7, the emerging flux within the filament channel increases the low-layer coronal field, which expands and reconnects with the field lines of the flux rope (*because of the “inverse polarity”!*). Therefore, more and more detached field lines become line-tied to the solar surface and the increased magnetic tension force pulls the flux rope down (*left panel*); the emerging flux on the outer edge pushes the global magnetic structure at one side far from the flux rope, and the flux rope is forced to move downward (*right panel*). So, the nonreconnecting flux both within the filament channel and on the outer edge of the channel makes the flux rope move downward, i.e., there is no occurrence of CMEs, which is in good agreement with

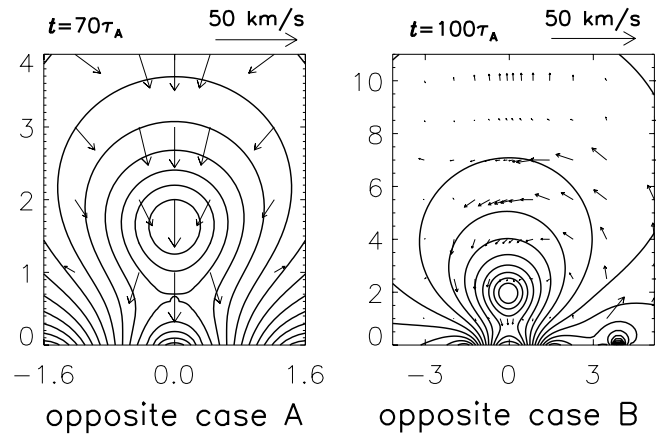


FIG. 7.—Situations opposite to cases A and B, i.e., with non-reconnecting emerging flux appearing within the filament channel and on the outer edge of the channel, respectively.

the observations by Feynman & Martin (1995). In particular, the reconnection process in the opposite of case A is a somewhat similar to that in Forbes & Priest (1984), who showed there is no upward eruption but static equilibrium after magnetic reconnection.

In other words, it is shown that if the background magnetic field is clockwise, anticlockwise emerging flux will trigger the CME (hereafter simply referred to as “+ effect”) when it is located within the filament channel (i.e., case A) and will push the flux rope down (hereafter simply referred to as “– effect”) when it is on the outer edge of the channel (i.e., the opposite of case B); conversely, clockwise emerging flux has a – effect when it is located within the filament channel (i.e., the opposite of case A) and a + effect when it is located on the outer edge of the channel (i.e., case B). Further simulations with different locations of the emerging flux indicate that from the filament channel center to the outer edge, the effect of anticlockwise emerging flux changes gradually from + to –, and oppositely, the effect of clockwise emerging flux changes gradually from – to +. These results perfectly explain why the emerging flux inside one of the single-polarity regions (between the center and the outer edge of the filament channel) was said to be neither favorably nor unfavorably oriented for CMEs (Feynman & Martin 1995). For certain emerging flux, its effect changes from one to the other as its location moves from the filament channel center to the outer edge of the channel.

4.2. Application to Low’s Filament Model

The localized small magnetic loops below the flux rope in our initial model do not necessarily exist for the inverse-polarity filaments, e.g., in Low’s model (Low 1994). In this case, the magnetic cancellation appearing in case A will not occur when reconnection-favored flux emerges within the filament channel. To get such an initial configuration, we shift our previous initial magnetic field downward by $\Delta y = 0.8$. As shown in Figure 8, when reconnection-favored flux emerges below the flux rope, it pushes the flux rope from its bottom since the emerging flux has the same direction as the field lines at the flux rope bottom. Moreover, emerging flux continues to reconnect with ambient coronal field lines at its two “shoulders,” which makes more line-tied field lines detached from the solar surface. The loss of

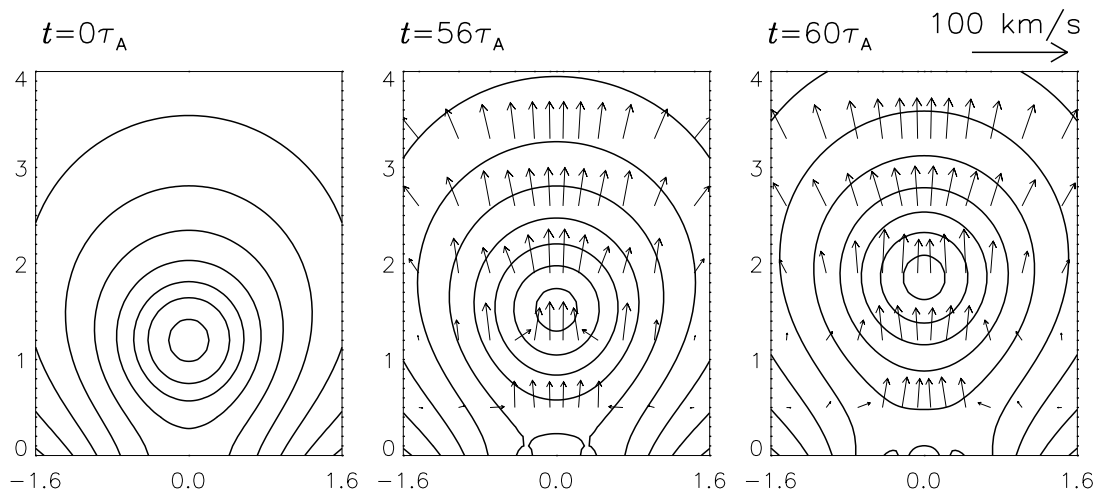


FIG. 8.—Response of magnetic structure with Low’s model-like initial magnetic configuration to the reconnection-favored emerging flux appearing within the filament channel.

line-tied constraint causes the flux rope to be accelerated upward and ejected away. This process is similar to that in Guo et al. (1996). When nonreconnecting flux emerges (here “nonreconnecting” is deduced from the magnetic polarities at the solar surface), it reconnects with the field lines at the flux rope bottom (owing to the “inverse-polarity”!), which removes the detached magnetic flux, while produces more and more line-tied field lines. The flux rope is pulled downward in a similar way to opposite case A (right panel of Fig. 7). Therefore, our trigger mechanism is also applicable to Low’s pre-CME model.

4.3. Conclusion

Observations show that CMEs are strongly correlated to two categories of reconnection-favored emerging flux (Feynman & Martin 1995). Motivated by the observed correlation and based on the erupting flux rope model, we

propose an emerging flux trigger mechanism for CMEs using numerical simulations, where

1. reconnection-favored emerging flux, either within the filament channel or on the outer edge of the channel, triggers the loss of equilibrium of the flux rope and the formation of a current sheet below the rope
2. the following fast magnetic reconnection in the current sheet leads to the eruption of the CME and the cusp-shaped solar flare or X-ray arcade.

One of the authors (PFC) thanks all the colleagues at Kwasan Observatory for their hospitality during his stay, and thanks B. C. Low for helpful discussions. P. F. C. is supported in part by a key project (No. 4990451) from the National Natural Science Foundation of China.

REFERENCES

- Aly, J. J. 1991, *ApJ*, 375, L61
 Amari, T., Luciani, J. F., Aly, J. J., & Mikić, Z. 1997, in *Coronal Mass Ejections*, ed. N. Crooker, J. A. Joselyn, & J. Feynman (Geophys. Monogr. 99: Washington, DC: AGU), 101
 Biskamp, D., & Welter, H. 1989, *Sol. Phys.*, 120, 49
 Chen, J., et al. 1997, *ApJ*, 490, L191
 Chen, P. F., Fang, C., Ding, M. D., & Tang, Y. H. 1999a, *ApJ*, 520, 853
 Chen, P. F., Fang, C., Tang, Y. H., & Ding, M. D. 1999b, *ApJ*, 513, 516
 Choe, G. S., & Lee, L. C. 1996, *ApJ*, 472, 360
 Datlowe, D. W., Elcan, M. J., & Hudson, H. S. 1974, *Sol. Phys.*, 39, 155
 Dere, K. P., Brueckner, G. E., Howard, R. A., Michels, D. J., & Delaboudiniere, J. P. 1999, *ApJ*, 516, 465
 Feynman, J., & Hundhausen, A. J. 1994, *J. Geophys. Res.*, 99, 8451
 Feynman, J., & Martin, S. F. 1995, *J. Geophys. Res.*, 100, 3355
 Finn, J. M., Guzdar, P. N., & Chen, J. 1992, *ApJ*, 393, 800
 Forbes, T. G. 1990, *J. Geophys. Res.*, 95, 11919
 Forbes, T. G., Isenberg, P. A., & Priest, E. R. 1994, *Sol. Phys.*, 150, 245
 Forbes, T. G., & Priest, E. R. 1984, *Sol. Phys.*, 94, 315
 ———. 1995, *ApJ*, 446, 377
 Gosling, J. T. 1993, *J. Geophys. Res.*, 98, 18937
 Guo, W. P., Wu, S. T., & Tandberg-Hanssen, E. 1996, *ApJ*, 469, 944
 Hanaoka, Y., et al. 1994, *PASJ*, 46, 205
 Harrison, R. A., Waggett, P. W., Bentley, R. D., Phillips, K. J. H., Bruner, M., Dryer, M., & Simnett, G. M. 1985, *Sol. Phys.*, 97, 387
 Hesse, M., Schindler, K., Birn, J., & Kuznetsova, M. 1999, *Phys. Plasma*, 6, 1781
 Heyvaerts, J., Priest, E. R., & Rust, D. M. 1977, *ApJ*, 216, 123
 Hiei, E., Hundhausen, A. J., & Sime, D. G. 1993, *Geophys. Res. Lett.*, 20, 2785
 Howard, R. A., et al. 1997, in *Coronal Mass Ejections*, ed. N. Crooker, J. A. Joselyn, & J. Feynman (Geophys. Monogr. 99: Washington, DC: AGU), 17
 Hu, Y. Q. 1989, *J. Comput. Phys.*, 84, 441
 Hudson, H. S., Acton, L. W., Harvey, K. L., & McKenzie, D. E. 1999, *ApJ*, 513, L83
 Hudson, H. S., Haisch, B., & Strong, K. T. 1995, *J. Geophys. Res.*, 100, 3473
 Hundhausen, A. 1999, *The Many Faces of the Sun*, ed. K. Strong, J. Saba, B. Haisch, & J. Schmelz (Berlin: Springer), 143
 Inhester, B., Birn, J., & Hesse, M. 1992, *Sol. Phys.*, 138, 257
 Kahler, S. W. 1992, *ARA&A*, 30, 113
 Kahler, S. W., Moore, R. L., Kane, S. R., Zirin, H. 1988, *ApJ*, 328, 824
 Kurokawa, H. 1987, *Space Sci. Rev.*, 51, 49
 ———. 1996, *IAU Colloq. 153, Magnetodynamic Phenomena in the Solar Atmosphere*, ed. Y. Uchida, T. Kosugi, & H. S. Hudson (Dordrecht: Kluwer), 185
 Low, B. C. 1994, *Phys. Plasma*, 1, 1684
 ———. 1996, *Sol. Phys.*, 167, 217
 ———. 1999, in *Solar Wind Nine*, ed. S. R. Habbal, R. Esser, J. V. Hollweg, & P. A. Isenberg, 109
 Low, B. C., & Smith, D. F. 1993, *ApJ*, 410, 412
 Magara, T., Shibata, K., & Yokoyama, T. 1997, *ApJ*, 487, 437
 Martin, S. F. 1990, in *Dynamics of Quiescent Prominences*, ed. V. Ruzdjak & E. Tandberg-Hanssen (Berlin: Springer), 1
 Mikić, Z., Barnes, D. C., & Schnack, D. D. 1988, *ApJ*, 328, 830
 Mikić, Z., & Linker, J. A. 1994, *ApJ*, 430, 898
 Ohya, M., & Shibata, K. 1997, *PASJ*, 49, 249
 Shibata, K. 1996, *Adv. Space Res.*, 17, 9
 Shibata, K., Nozawa, S., & Matsumoto, R. 1992, *PASJ*, 44, 265
 Sturrock, P. A. 1991, *ApJ*, 380, 655
 Tajima, T., & Shibata, K. 1997, *Plasma Astrophysics* (Reading: Addison: Wesley)
 Tandberg-Hanssen, E. 1995, *The Nature of Solar Prominences* (Dordrecht: Kluwer.), 267

- Tsuneta, S. 1997, ApJ, 483, 507
Tsuneta, S., et al. 1992, PASJ, 44, L211
Ugai, M. 1982, Phys. Fluids, 25, 1027
van Ballegooijen, A. A., & Martens, P. C. H. 1989, ApJ, 343, 971
Wang, Y. M., & Sheeley Jr, N. R. 1999, ApJ, 510, L157
Wood, B. E., Karovska, M., Chen, J., Brueckner, B. G., Cook, J. W., & Howard, R. A. 1999, ApJ, 512, 484
- Wu, S. T., & Guo, W. P. 1997, in Coronal Mass Ejections, ed. N. Crooker, J. A. Joselyn, & J. Feynman (Geophys. Monogr. 99: Washington, DC: AGU), 83
Yokoyama, T., & Shibata, K. 1996, PASJ, 48, 353